Accepted Manuscript

Title: Sodium ion storage in reduced graphene oxide

Author: Ashok Kumar Nanjundan Rohit Ranganathan Gaddam Srinivasa Rao Varanasi Dongfang Yang Suresh K. Bhatia X.S. Zhao

PII: S0013-4686(16)31768-6
DOI: http://dx.doi.org/doi:10.1016/j.electacta.2016.08.058
Reference: EA 27836

To appear in: *Electrochimica Acta*

Received date: 12-7-2016
Revised date: 9-8-2016
Accepted date: 12-8-2016

Please cite this article as: Ashok Kumar Nanjundan, Rohit Ranganathan Gaddam, Srinivasa Rao Varanasi, Dongfang Yang, Suresh K.Bhatia, X.S.Zhao, Sodium ion storage in reduced graphene oxide, Electrochimica Acta http://dx.doi.org/10.1016/j.electacta.2016.08.058

Sodium ion storage in reduced graphene oxide

Nanjundan Ashok Kumar,[†]* Rohit Ranganathan Gaddam,[†] Srinivasa Rao Varanasi, Dongfang Yang, Suresh K. Bhatia and X. S. Zhao*

School of Chemical Engineering, The University of Queensland, St Lucia, Brisbane 4072 Australia.

† Authors contributed equally

* Corresponding authors: E-mail: george.zhao@uq.edu.au, ashok.nanjundan@uq.edu.au

Abstract

The performance of few-layered metal-reduced graphene oxide (RGO) as a negative electrode material in sodium-ion battery was investigated. Experimental and simulation results indicated that the as-prepared RGO with a large interlayer spacing and disordered structure enabled significant sodium-ion storage, leading to a high discharge capacity. The strong surface driven interactions between sodium ions and oxygen-containing groups and/or defect sites led to a high rate performance and cycling stability. The RGO anode delivered a discharge capacity of 272 mA h g^{-1} at a current density of 50 mA g^{-1}, a good cycling stability over 300 cycles and a superior rate capability. The present work provides new insights into optimizing RGOs for high-performance and low-cost sodium-ion batteries.

Keywords: Graphene oxide; Metal reduction; Anode; Sodium-ion battery; Stability

Introduction

Rechargeable lithium-ion batteries (LIBs) are ubiquitous in the modern world [1]. However, large-scale application of LIBs might face certain constraints due to the uneven geographical distribution of lithium resources [2]. Sodium-ion batteries (NIBs) are an alternative to LIBs. Sodium is an earth abundant element that has the capacity to replace the existing LIB technology for large-scale applications [3]. One particular disadvantage of sodium is its relatively larger ionic radius than lithium (1.02 Å of Na^+ *vs.* 0.76 Å of Li^+), thus requiring larger channels for transport and interstitial sites for sodium ions [4]. Recent research has been

focusing on identifying and developing suitable electrode materials for the sodium-ion energy storage technology. While a number of cathode materials for NIBs have been investigated in the past [3, 5], there have been only a few anode materials that are suitable for NIBs. Pristine sodium metal as anode (gravimetric capacity of 1165 mA h g^{-1}) leads to the formation of dendrites, causing thermal runaway [6]. Alternative anodes such as carbonaceous materials [7], transition metal oxides [8], metal nitrides [9] and alloys [10, 11] have been studied. Among them, carbon nanomaterials are promising owing to their earth abundance, low cost, and good electric conductivity [7]. Unfortunately, the commonly used graphite anode for LIBs shows a low reversible capacity for sodium ions (35 mA h g^{-1}) because of small interlayer spacing (3.4 Å) [12], which is lower than the critical interlayer distance for Na^+ insertion (3.7 Å) [13].

Few layered graphene nanosheets with large surface area, chemical stability, and excellent electronic conductivity, holds great promise as an electrode material for electrochemical energy storage systems. The use of such graphene nanosheets as electrode materials for NIBs, although not as prevalent in the literature as for LIBs, have started to emerge recently [14-19]. It has been demonstrated that thermally reduced graphene oxide (RGO) with a *d*-spacing of 3.7 Å displayed a specific capacity of 174 mA h g^{-1} at a current density of 40 mA g^{-1} [15]. The capacity was further increased to 280 mA h g^{-1} at a current density of 20 mA g^{-1} by expanding the interlayer spacing to 4.3 Å [20]. The above results indicate that RGO has the potential to be used as anode for NIBs.

The chemical exfoliation method remains a cost-effective approach to mass production of graphene oxide (GO) from graphite. However, the reduction of GO to RGO relies heavily on using toxic reductants like hydrazine hydrate, [21] sodium borohydride, [22] potassium carbonate [23] among many others [24]. Besides, majority of the reduction strategies either involves the use of high temperatures and/or multi-step time consuming processes [24, 25].

Recently, Kumar *et al.* [26] demonstrated a simple and fast method for the production of RGO at room temperature by using tin (II) chloride as a reducing agent in a strongly acidic medium. In this work, we investigated the electrochemical properties of thus reduced RGO, which was used as anode in NIBs. Experimental results showed that the RGO anode can deliver a specific discharge capacity of 272 mA h g^{-1} at 50 mA g^{-1} (second cycle) with a good cycling stability and a superior rate capability. For comparison, we also prepared RGO using iron (Fe) metal powder as a reducing agent [27]. Both experimental and computer-simulation data indicate that the energy storage mechanism is surface-driven, where reactions between Na^+ and the defects on the surface of RGOs advantageously influence the interfacial activity between electrode and electrolyte.

Experimental section

GO was synthesised using graphite powder (400 nm; 99.99% metal base) by using a modified Hummers and Offeman's method [28, 29]. GO was deoxygenated using metal salt, tin (II) chloride, [26] and a metal powder, iron (Fe) [27] to yield Sn-RGO and Fe-RGO, respectively. In a typical procedure, 0.6 g of GO was dispersed in 600 mL of distilled water and sonicated for 60 min. Then, 6 g of the reductant, either, tin (II) chloride or Fe powder was added to the mixture along with 100 mL of hydrochloric acid (32% HCl). The mixture was stirred for 30 min and left overnight. After reduction, 75 mL of HCl was added in excess and washed with copious amounts of water and then with ethanol. This product was isolated by membrane filtration, washed with ethanol again and dried under vacuum at 90 °C overnight. (*Note: repeated and prolonged washing with concentrated HCl (highly acidic medium) will remove traces of reductants*) [26, 30].

Material characterization

X-ray diffraction (XRD) was carried out on a Bruker D8 Advance X-ray diffractometer with Ni-filtered Cu Kα radiation (λ = 1.54056 Å; 40 kV, 30 mA). The morphology of the prepared samples was examined by using a field emission scanning electron microscope (FE-SEM, JEOL 7001) and transmission electron microscope (TEM, JEOL 2100) at an acceleration voltage of 200 kV. X-ray photoelectron spectroscopy (XPS) spectra were acquired on a Kratos Axis ULTRA X-ray photoelectron spectrometer. Raman spectra were collected using a Renishaw Raman Spectrometer fitted with a 514 nm laser. The specific surface areas of samples were calculated using the BET method from the adsorption isotherms measured on a Tristar II 3020. All samples were degassed at 150 °C for 3 h prior to the measurement.

Electrode fabrication and electrochemical measurements

A conventional slurry-coating process was applied to fabricate the electrodes. The active material (Sn-RGO or Fe-RGO), carbon black and polyvinyldine fluoride (PVdF) were mixed in a mass ratio of 7:2:1 and homogenized in *N*-methyl pyrrolidine (NMP) to form a slurry, which was subsequently coated on a Cu foil current collector, followed by drying at 60 °C overnight under vacuum. The total mass loading on each electrode was controlled to be ~1.5 mg.

2032-type coin cells were assembled in an argon-filled glove-box, using a glass fiber as the separator, sodium foil as the counter electrode, 1 M $NaClO_4$ in a 1:1 (v/v) mixture of ethylene carbonate (EC) and propylene carbonate (PC) mixed with 0.3 wt% of fluoroethylene carbonate (FEC) additive as the electrolyte. *The FEC additive is capable of the electrochemical deposition/dissolution of metallic Na with higher reversibility because of improved passivation and suppression of side reactions between Na metal and propylene carbonate solution containing Na salts* [31]. Cyclic voltammetric (CV) measurements were carried out on a CHI-600D electrochemical workstation using cutoff voltages between 0.005 and 3V versus Na/Na^+ at a scan rate of 0.2 mV s^{-1}. The galvanostatic charge/discharge measurements were performed

on NEWARE BTS-CT3008 (Neware Technology, Ltd., Shenzhen, China) at different current densities. Electrochemical impedance spectroscopy measurement was conducted on a CHI-600D electrochemical workstation in the frequency range of 100 kHz to 10 mHz. All electrochemical measurements were carried out at room temperature.

Computational simulations

Density functional theory (DFT) calculations were performed on a triangular lattice of graphene consisting 128 carbon atoms with a single Stone-Thrower-Wales (STW or SW) [32, 33] or double vacancy (DV) defects using Vienna Ab initio Simulation Package (VASP) [34-37]. The projector augmented wave (PAW) method and the Perdue-Burke-Ernzerhof (PBE) form of the generalized gradient approximation (GGA) for exchange and correlation functional were used [38]. In order to avoid the spurious interactions between periodic images of graphene sheets, an empty space of 2 nm along the direction perpendicular to the graphene plane was introduced. An energy cut-off 400 eV was set for the plane wave expansion of wave functions. A randomly selected C-C bond was rotated by 90^{o} to create an SW defect and a pair of carbons was removed to create DV defect and the structures were optimized subsequently. For each loading of sodium atoms, 5 different random configurations were used for DFT calculations and lowest energy configuration was selected among them for adsorption energy calculation.

Results and discussion

Figures 1(a) and (c) show the FESEM images of Fe-RGO and Sn-RGO. Thin layers of graphene sheets can be clearly seen. The sheets overlapped on one another and displayed a wrinkled structure leading to nano-cavities, which is favorable for sodium-ion insertion/adsorption [15]. The representative TEM images of the two samples are shown in **Figure 1(b)** and (**d)**. Again, thin transparent, silk veil-like nanosheets with some crumpled or thicker ripples can be seen, indicating the presence of few-layered graphene sheets.

Figure 2a shows the XRD patterns of graphite, GO and RGOs. As can be seen, a characteristic (002) peak for graphitic carbon appeared at ca. 26° (2θ), corresponding to a layer-to-layer distance (*d*-spacing) of ~0.34 nm. The interlayer spacing was increased to 0.79 nm in the GO sample with a shift in 2θ to 11.2° due to the formation of interlayer oxygen-containing groups. Two diffraction peaks at ~24° (2θ) corresponding to (002) plane of layered graphite and ~43° (2θ) corresponding to (100) plane of graphite can be observed from both RGO samples. The absence of peak at ~11°suggests the reduction of GO to RGO. Compared to the *d*-spacing of 0.34 nm for graphite, the *d*-spacing of Sn-RGO was 0.378 nm, which is slightly higher than that of Fe-RGO (*d*-spacing = 0.367 nm). The low signal to background ratio is attributed to incoherent scattering in the poorly crystallized, randomly stacked few-layered RGOs, suggesting a high degree of disorder [15]. This low crystallization is predominantly due to the formation of surface oxygen-containing functional groups arising during graphite oxidation and deoxygenation. This increase in *d*-spacing and a certain degree of disorder is important for the insertion/extraction of the relatively large sodium ions.

The Raman spectra of graphite, GO and RGOs are shown in **Figure 2b**. Both the RGOs revealed the pronounced D and G bands at around ~1342 cm^{-1} and ~1576 cm^{-1} respectively. A D' band at 1620 cm^{-1} can be observed from both GO and RGOs. This band arises from the edge reconstruction and dangling bonds present in the sp^2 carbons [39, 40]. In general, this band appears as a shoulder for G-band at the higher frequency region [41]. It can be observed that the intensity of this band decreases in the case of the as prepared RGOs when compared to that of GO. The I_D/I_G ratio of Fe-RGO is 1.19 and Sn-RGO is 1.14, which are higher than that of graphite (I_D/I_G = 0.34), indicating a highly disordered nature of the RGO sheets and the

associated unrepaired edge defects [4]. These results are in coherence with the XRD and FESEM data.

The deoxygenation of GO along with evaluation of the respective chemical composition were estimated using the XPS technique. **Figure S1** shows the XPS data of graphite, GO, Sn-RGO and Fe-RGO**.** The oxygen content of ~3 at% in graphite could have originated from the edge terminating oxygen functional group in the grain and lattice boundaries of graphite [42] (**Table S1**). On the other hand, the oxygen content in GO was ~27 at%. After reduction, Sn-RGO contained 9 at% and Fe-RGO contained 8 at% of oxygen, respectively, which indicated a fair reduction of GO to RGO by tin (II) chloride and metallic iron. The functional groups presented on both the RGOs seem to be similar (**Figure S2**). The high resolution C1s spectra were deconvoluted into a dominant component of C-C (sp^2), C-C (sp^3), C-O and C=O at binding energies of ~284.60, ~286.02, ~286.99 and ~288.32 eV respectively [43]. Also a π-π^* peak with a broadening on the high energy side, typical to that of graphitic carbons could also be observed at ~290.12 eV [44]. Similarly, the high resolution scan of O1s peaks corresponding to OH, O=C and O-C at binding energies of ~531.42, ~532.47 and ~533.47 eV respectively were observed. The adsorbed atmospheric moisture could be visualised as a peak at ~534.73 eV respectively. Furthermore, the elemental mapping images of Sn-RGO and Fe-RGO demonstrate the uniform distribution of carbon and oxygen throughout the material (**Figure S3 and S4**). The BET surface area of GO was 55 m^2/g. Upon reduction, the surface area increased to 198 and 124 m^2/g for Sn-RGO and Fe-RGO, respectively.

Electrochemical performance vs Na/Na^+

The sodium-ion storage behaviour of the as prepared RGO was evaluated through cyclic voltammetry (CV), electrochemical impedance spectroscopy (EIS) and glavanostatic

discharge/charge (GDC) techniques using a half cell setup with sodium foil as a counter electrode. **Figure 3** presents the CV curves of the RGOs carried out at 0.2 mV s^{-1} in the voltage range of 0.005 – 3V. A pronounced reduction peak at 0.82 and 0.92 V can be seen from Fe-RGO and Sn-RGO, respectively. This reduction peak was due to the degradation of the electrolyte and the formation of solid electrolyte interphase (SEI) [45]. A sharp cathodic peak near ~0.015 V was observed for both RGOs. Nevertheless, no corresponding anodic peak can be observed, indicating an adsorption mechanism for sodium-ion storage on the graphene sheets or unrepaired defect sites [15, 46]. In addition, a pair of redox peaks were observed at 0.8 and 2.5 V indicating sodium-ion interaction with surface oxygen containing functional groups or impurities [47]. After a couple of cycles, the CVs were stable and rectangular shaped in the higher potential region. This indicates a capacitive storage behaviour attributed to electro-adsorption/desorption of sodium-ions in RGOs [17, 48]. Also, the overlapping of the CV curves in the subsequent cycles is indicative of good battery stability and reversible sodium-ion interaction. From the CV curves, the storage behaviour of sodium-ions in both the RGOs seems to be similar to that of lithium-ions in graphitic-carbon [49]. As a result, it can be concluded that the mechanism of sodium-ion interactions with the RGOs is likely to involve chemisorption on hetero-atoms, filling of nanopores and reversible surface physical adsorption [50].

Figure 4 reproduces the discharge/charge profiles for both the RGOs at 50 mA g^{-1} in the voltage range of 0.005-3V. In the initial cycle a specific discharge and charge capacity of 735 and 192 mA h g^{-1} respectively was obtained for Fe-RGO. In the case of Sn-RGO, the initial discharge and charge capacity was 819 and 259 mA h g^{-1} respectively. The Coulombic efficiency (CE) in the first cycle for Fe-RGO and Sn-RGO was poor due to the formation of SEI and irreversible insertion of sodium-ion in vacancies and defect sites as commonly

observed in many carbon samples (**Figures 4(b) and (e))** [51]. This phenomenon also resonates with that of the CV measurements. In spite of the relatively low CE in the first cycle, the RGO electrodes exhibited much higher average CE of 95% after 20 cycles as an indication of the system's stability during cycling. The charge-discharge profiles of both RGOs show sloping curves [15]. This behaviour is an indication of physical interaction of sodium ion with RGO. Such sloping behaviour can be accredited to the reversible interaction of sodium at vacancies and Stone-Wales (SW) defects [4]. The Fe-RGO and Sn-RGO showed a specific discharge capacity of 202 and 272 mA h g^{-1} in the second cycle respectively. Upon repeated cycling, the CE nearly reached 99% with a discharge capacity of 140 and 154 mA h g^{-1} at the 50^{th} cycle (**Figures 4(b) and (e)**, **Table S2**). The batteries were stable over 300 cycles when measured at a current density of 50 mA g^{-1}. The rate performance of the as-prepared RGOs *vs.* sodium was investigated by charging and discharging the battery at various current densities ranging from 0.1 to 1 A g^{-1} as shown in **Figure 4(c) and (d)**. Sn-RGO delivered discharge capacities of ~268, ~146, ~109, ~88, ~66 and ~59 mA h g^{-1} at 0.05, 0.1, 0.2, 0.4, 0.8 and 1 A g^{-1} current densities respectively. In case of Fe-RGO *vs.* Na/Na^+, discharge capacities of ~204, ~141, ~117, ~103 and ~86 mA h g^{-1} were obtained at 0.05, 0.1, 0.2, 0.4 and 0.8 A g^{-1} respectively (**Figure S5**). Sn-RGO delivered a slightly better performance than Fe-RGO. This can be attributed to the higher interlayer spacing observed in Sn-RGO.

The EIS profiles of Fe-RGO and Sn-RGO are presented in **Figure 5.** A Nyquist plot representing depressed semicircle in the high frequency region and a straight line in the low frequency region is observed. The modelling of the EIS data was carried out using the equivalent circuit represented in the inset in **Figure 5.** Here, R_e represents the resistance arising

from electrolytes and contacts. C_{LC} signifies a double layer capacitance, R_{ct} is the charge-transfer resistance, Z_w is the Warburg impedance (associated with sodium ion diffusion in RGO electrode). During the initial cycle a thick passivating layer of SEI is formed that offers a parallel combination of resistance, R_{SEI} and a capacitance, C_{SEI} [4]. The numerical values obtained from modelling are shown in **Table S3**. The overall resistance R_c+R_{SEI} seems to be less in case of Fe-RGO as compared to Sn-RGO.

The performance of the RGOs prepared by metal induced reduction of GO with that of RGOs prepared using various chemical and thermal reduction techniques are compared in **Table 1**. Although only a few studies report the direct use of RGO as anodes for NIBs, our results are comparable or better than most of the RGOs reported in the literature. We note that only few studies have achieved capacities nearing 200 mA h g^{-1} at much lower current densities (**Table 1**). In addition, the room temperature reduction strategy used in our approach is environmentally benign and mild when compared to other strategies which require high thermal energy and toxic reductants.

To further analyze how the Na^+ interacts with RGO, DFT calculations were performed. **Figures 6(a) and (b)** depict the snapshot of the relaxed structures of the adsorbed Na atoms on the graphene sheet with one SW and DV defects. It clearly shows that Na atoms tend to adsorb close to the defect sites rather than those away from the defects. In each of these cases, energy of adsorption was calculated using [53, 54]:

$$E_{ads} = E_{graphene} + n_{Na}E_{Na} - E_{Na-graphene} \quad (1)$$

where n_{Na} is the number of Na atoms, $E_{graphene}$, E_{Na} and $E_{Na\text{-}graphene}$ are the total energies

associated with graphene lattice alone (no Na atoms adsorbed), Na atom on a body centre cubic (bcc) lattice and a system with n_{Na} Na atoms adsorbed on graphene lattice respectively. **Figure 6c** shows the variation adsorption energy as a function of amount of Na atoms adsorbed on the graphene sheet with SW and DV defects. Positive value of adsorption energy indicates favourable configuration of adsorbate-adsorbent combination. The positive value of this quantity decreases to zero with increase in the amount Na atoms and becomes negative when the amount of Na is further increased. The amount of Na corresponding to the adsorption energy when it starts changing its sign is the maximum amount of Na that can be adsorbed onto any given amount of the carbon. In the present case, the maximum amount of adsorbed Na is 11.5% and 16.75% for SW and DV defects respectively. From these value, one can estimate the maximum capacity of NIB with defective graphene anode using [53]:

$$C_{Na-graphene} = \frac{A_{Na} vF}{M_C} x1000 \qquad (2)$$

where A_{Na}, ν, F and M_C represent maximum amount of Na, valency of Na ion, Faraday constant (26.801 Ah/mole) and atomic mass of the carbon (12.011). In the present case, the maximum capacity is estimated to be 256.84 and 374.1 mA h g^{-1} for SW and DV defects respectively. The value estimated for SW defect is pretty close to what we have measured for RGO. However, we note that RGO contains mostly a mixture of SW and DV along with oxygen functional groups. Therefore, our estimate of capacity from DFT calculations is reasonable and paves the way to get closer estimates when defects of other kind are incorporated in the calculations.

Results from DFT calculations indicate that defect sites in graphene and allied allotropes are favourable for Na adsorption. They also reveal that one can get a reasonable estimate for Na storage capacity of graphene anodes even in presence of tiny amount SW

defects. Therefore, we conclude that DFT calculations are quite helpful in optimizing carbons such as graphene for better performance in energy storage applications.

Conclusion

Highly reduced graphene oxide was produced by using metals as reducing agents. Tin (II) chloride reduced GO (Sn-RGO) and iron reduced GO (Fe-RGO) when tested as anode for sodium-ion battery respectively delivered a specific discharge capacity of 272 and 202 $mAhg^{-1}$ at current density of 50 mA g^{-1}in the second cycle. The observed higher capacity of Sn-RGO in comparison with that of Fe-RGO is attributed to the wider interlayer spacing of RGO. The present work provides new insights into optimising the electrochemical performance of RGOs for sodium-ion batteries. The experimental and computational findings strongly suggest that defects significantly enhance the sodium storage capability in RGOs.

Acknowledgements

This research was supported by the University of Queensland under the Vice-Chancellor's Research and Teaching Fellowship Program (2015000144). RRG acknowledges the scholarships granted by The University of Queensland. NAK thanks the University of Queensland for UQ fellowship. The authors gratefully acknowledge the facilities and technical assistance of the Australian Microscopy and Microanalysis Research Facility at the UQ Centre for Microscopy and Microanalysis.

Appendix A. Supplementary material

Supplementary data associated with this article can be found in the online version at http://dx.doi.org/xxx.

References

[1] J.B. Goodenough, K.-S. Park, The Li-Ion Rechargeable Battery: A Perspective, J. Am. Chem. Soc., 135 (2013) 1167-1176.

[2] R.R. Gaddam, D. Yang, R. Narayan, K. Raju, N.A. Kumar, X.S. Zhao, Biomass derived carbon nanoparticle as anodes for high performance sodium and lithium ion batteries, Nano Energy, 26 (2016) 346-352.

[3] D. Kundu, E. Talaie, V. Duffort, L.F. Nazar, The Emerging Chemistry of Sodium Ion Batteries for Electrochemical Energy Storage, Angew. Chem., Int. Ed., 54 (2015) 3431-3448.

[4] E.M. Lotfabad, J. Ding, K. Cui, A. Kohandehghan, W.P. Kalisvaart, M. Hazelton, D. Mitlin, High-Density Sodium and Lithium Ion Battery Anodes from Banana Peels, ACS Nano, 8 (2014) 7115-7129.

[5] L.P. Wang, L. Yu, X. Wang, M. Srinivasan, Z.J. Xu, Recent developments in electrode materials for sodium-ion batteries, J. Mater. Chem. A, 3 (2015) 9353-9378.

[6] M.D. Slater, D. Kim, E. Lee, C.S. Johnson, Sodium-Ion Batteries, Advanced Functional Materials, 23 (2013) 947-958.

[7] M.-S. Balogun, Y. Luo, W. Qiu, P. Liu, Y. Tong, A review of carbon materials and their composites with alloy metals for sodium ion battery anodes, Carbon, 98 (2016) 162-178.

[8] H. Su, S. Jaffer, H. Yu, Transition metal oxides for sodium-ion batteries, Energy Storage Mater., 5 (2016) 116-131.

[9] X. Li, M.M. Hasan, A.L. Hector, J.R. Owen, Performance of nanocrystalline Ni3N as a negative electrode for sodium-ion batteries, J. Mater. Chem. A, 1 (2013) 6441-6445.

[10] Y. Kim, Y. Park, A. Choi, N.S. Choi, J. Kim, J. Lee, J.H. Ryu, S.M. Oh, K.T. Lee, An amorphous red phosphorus/carbon composite as a promising anode material for sodium ion batteries, Adv. Mater., 25 (2013) 3045-3049.

[11] L. Wu, X. Hu, J. Qian, F. Pei, F. Wu, R. Mao, X. Ai, H. Yang, Y. Cao, Sb-C nanofibers with long cycle life as an anode material for high-performance sodium-ion batteries, Energy Environ. Sci., 7 (2014) 323-328.

[12] P. Ge, M. Fouletier, Electrochemical intercalation of sodium in graphite, Solid State Ionics, 28 (1988) 1172-1175.

[13] Y. Cao, L. Xiao, M.L. Sushko, W. Wang, B. Schwenzer, J. Xiao, Z. Nie, L.V. Saraf, Z. Yang, J. Liu, Sodium Ion Insertion in Hollow Carbon Nanowires for Battery Applications, Nano Lett., 12 (2012) 3783-3787.

[14] Y. Yan, Y.-X. Yin, Y.-G. Guo, L.-J. Wan, A Sandwich-Like Hierarchically Porous Carbon/Graphene Composite as a High-Performance Anode Material for Sodium-Ion Batteries, Adv. Energy Mater., 4 (2014) n/a-n/a.

[15] Y.-X. Wang, S.-L. Chou, H.-K. Liu, S.-X. Dou, Reduced graphene oxide with superior cycling stability and rate capability for sodium storage, Carbon, 57 (2013) 202-208.

[16] Y.S. Yun, Y.-U. Park, S.-J. Chang, B.H. Kim, J. Choi, J. Wang, D. Zhang, P.V. Braun, H.-J. Jin, K. Kang, Crumpled graphene paper for high power sodium battery anode, Carbon, 99 (2016) 658-664.

[17] X.-F. Luo, C.-H. Yang, Y.-Y. Peng, N.-W. Pu, M.-D. Ger, C.-T. Hsieh, J.-K. Chang, Graphene nanosheets, carbon nanotubes, graphite, and activated carbon as anode materials for sodium-ion batteries, J. Mater. Chem. A, 3 (2015) 10320-10326.

[18] J.C. Pramudita, D. Pontiroli, G. Magnani, M. Gaboardi, M. Riccò, C. Milanese, H.E.A. Brand, N. Sharma, Graphene and Selected Derivatives as Negative Electrodes in Sodium- and Lithium-Ion Batteries, ChemElectroChem, 2 (2015) 600-610.

[19] L. David, G. Singh, Reduced Graphene Oxide Paper Electrode: Opposing Effect of Thermal Annealing on Li and Na Cyclability, J. Phys. Chem. C, 118 (2014) 28401-28408.

[20] Y. Wen, K. He, Y. Zhu, F. Han, Y. Xu, I. Matsuda, Y. Ishii, J. Cumings, C. Wang, Expanded graphite as superior anode for sodium-ion batteries, Nat. Commun., 5 (2014) 4033.

[21] S. Stankovich, D.A. Dikin, R.D. Piner, K.A. Kohlhaas, A. Kleinhammes, Y. Jia, Y. Wu, S.T. Nguyen, R.S. Ruoff, Synthesis of graphene-based nanosheets via chemical reduction of exfoliated graphite oxide, Carbon, 45 (2007) 1558-1565.

[22] H.-J. Shin, K.K. Kim, A. Benayad, S.-M. Yoon, H.K. Park, I.-S. Jung, M.H. Jin, H.-K. Jeong, J.M. Kim, J.-Y. Choi, Y.H. Lee, Efficient Reduction of Graphite Oxide by Sodium Borohydride and Its Effect on Electrical Conductance, Adv. Funct. Mater., 19 (2009) 1987-1992.

[23] D. He, Z. Peng, W. Gong, Y. Luo, P. Zhao, L. Kong, Mechanism of a green graphene oxide reduction with reusable potassium carbonate, RSC Adv., 5 (2015) 11966-11972.

[24] S. Pei, H.-M. Cheng, The reduction of graphene oxide, Carbon, 50 (2012) 3210-3228.

[25] C.K. Chua, M. Pumera, Chemical reduction of graphene oxide: a synthetic chemistry viewpoint, Chem. Soc. Rev., 43 (2014) 291-312.

[26] N.A. Kumar, S. Gambarelli, F. Duclairoir, G. Bidan, L. Dubois, Synthesis of high quality reduced graphene oxide nanosheets free of paramagnetic metallic impurities, J. Mater. Chem. A, 1 (2013) 2789-2794.

[27] N.A. Kumar, M. Togami, Y. Oishi, M. Tominaga, M. Takafuji, H. Ihara, Iron metal induced deoxygenation of graphite oxide nanosheets-insights on the capacitive properties of binder-free electrodes, RSC Adv., 5 (2015) 23367-23373.

[28] W.S. Hummers Jr, R.E. Offeman, Preparation of graphitic oxide, J. Am. Chem. Soc., 80 (1958) 1339-1339.

[29] N.A. Kumar, H.-J. Choi, Y.R. Shin, D.W. Chang, L. Dai, J.-B. Baek, Polyaniline-Grafted Reduced Graphene Oxide for Efficient Electrochemical Supercapacitors, ACS Nano, 6 (2012) 1715-1723.

[30] M. Zhang, D. Lei, Z. Du, X. Yin, L. Chen, Q. Li, Y. Wang, T. Wang, Fast synthesis of SnO2/graphene composites by reducing graphene oxide with stannous ions, J. Mater. Chem., 21 (2011) 1673-1676.

[31] S. Komaba, T. Ishikawa, N. Yabuuchi, W. Murata, A. Ito, Y. Ohsawa, Fluorinated Ethylene Carbonate as Electrolyte Additive for Rechargeable Na Batteries, ACS Appl. Mater. Int., 3 (2011) 4165-4168.

[32] A.J. Stone, D.J. Wales, Theoretical studies of icosahedral C60 and some related species, Chem. Phys. Lett., 128 (1986) 501-503.

[33] P. Thrower, Study of defects in graphite by transmission electron microscopy, Chem. Phys. Carbon 5 (1969) 217-320.

[34] G. Kresse, J. Hafner, {Ab initio} molecular dynamics for liquid metals, Phys. Rev. B, 47 (1993) 558-561.

[35] G. Kresse, J. Hafner, Ab initio molecular-dynamics simulation of the liquid-metal–amorphous-semiconductor transition in germanium, Phys. Rev. B, 49 (1994) 14251.

[36] G. Kresse, J. Furthmüller, Efficiency of ab-initio total energy calculations for metals and semiconductors using a plane-wave basis set, Comput. Mater. Sci., 6 (1996) 15-50.

[37] G. Kresse, J. Furthmüller, Efficient iterative schemes for ab initio total-energy calculations using a plane-wave basis set, Phys. Rev. B, 54 (1996) 11169.

[38] J.P. Perdew, K. Burke, M. Ernzerhof, Generalized gradient approximation made simple, Phys. Rev. Lett., 77 (1996) 3865.

[39] L.M. Malard, M.A. Pimenta, G. Dresselhaus, M.S. Dresselhaus, Raman spectroscopy in graphene, Phys. Rep., 473 (2009) 51-87.

[40] H. Liu, L. Zhang, Y. Guo, C. Cheng, L. Yang, L. Jiang, G. Yu, W. Hu, Y. Liu, D. Zhu, Reduction of graphene oxide to highly conductive graphene by Lawesson's reagent and its electrical applications, J. Mater. Chem. C, 1 (2013) 3104-3109.

[41] R.K. Biroju, P.K. Giri, Defect Enhanced Efficient Physical Functionalization of Graphene with Gold Nanoparticles Probed by Resonance Raman Spectroscopy, J. Phys. Chem. C, 118 (2014) 13833-13843.

[42] T. Szabó, O. Berkesi, P. Forgó, K. Josepovits, Y. Sanakis, D. Petridis, I. Dékány, Evolution of Surface Functional Groups in a Series of Progressively Oxidized Graphite Oxides, Chem. Mater., 18 (2006) 2740-2749.

[43] M. Koinuma, H. Tateishi, K. Hatakeyama, S. Miyamoto, C. Ogata, A. Funatsu, T. Taniguchi, Y. Matsumoto, Analysis of reduced graphene oxides by X-ray photoelectron spectroscopy and electrochemical capacitance, Chem. Lett., 42 (2013) 924-926.

[44] H. Estrade-Szwarckopf, XPS photoemission in carbonaceous materials: a “defect” peak beside the graphitic asymmetric peak, Carbon, 42 (2004) 1713-1721.

[45] E. Lim, C. Jo, M.S. Kim, M.H. Kim, J. Chun, H. Kim, J. Park, K.C. Roh, K. Kang, S. Yoon, J. Lee, High-Performance Sodium-Ion Hybrid Supercapacitor Based on Nb2O5@Carbon Core-Shell Nanoparticles and Reduced Graphene Oxide Nanocomposites, Adv. Funct. Mater., 26 (2016) 3711-3719.

[46] X. Zhou, Y.-G. Guo, Highly Disordered Carbon as a Superior Anode Material for Room-Temperature Sodium-Ion Batteries, ChemElectroChem, 1 (2014) 83-86.

[47] J. Xu, M. Wang, N.P. Wickramaratne, M. Jaroniec, S. Dou, L. Dai, High-performance sodium ion batteries based on a 3D anode from nitrogen-doped graphene foams, Adv Mater, 27 (2015) 2042-2048.

[48] H. Wang, W. Yu, J. Shi, N. Mao, S. Chen, W. Liu, Biomass derived hierarchical porous carbons as high-performance anodes for sodium-ion batteries, Electrochim. Acta, 188 (2016) 103-110.

[49] K. Tang, R.J. White, X. Mu, M.-M. Titirici, P.A. van Aken, J. Maier, Hollow Carbon Nanospheres with a High Rate Capability for Lithium-Based Batteries, ChemSusChem, 5 (2012) 400-403.

[50] D.A. Stevens, J.R. Dahn, High Capacity Anode Materials for Rechargeable Sodium-Ion Batteries, J. Electrochem. Soc., 147 (2000) 1271-1273.

[51] S. Wenzel, T. Hara, J. Janek, P. Adelhelm, Room-temperature sodium-ion batteries: Improving the rate capability of carbon anode materials by templating strategies, Energy & Environ. Sci., 4 (2011) 3342-3345.

[52] A. Ramos, I. Cameán, N. Cuesta, C. Antuña, A.B. García, Expanded graphitic materials prepared from micro- and nanometric precursors as anodes for sodium-ion batteries, Electrochim. Acta, 187 (2016) 496-507.

[53] D. Datta, J. Li, V.B. Shenoy, Defective Graphene as a High-Capacity Anode Material for Na- and Ca-Ion Batteries, ACS Appl. Mater. Int., 6 (2014) 1788-1795.

[54] X. Wang, G. Li, F.M. Hassan, J. Li, X. Fan, R. Batmaz, X. Xiao, Z. Chen, Sulfur covalently bonded graphene with large capacity and high rate for high-performance sodium-ion batteries anodes, Nano Energy, 15 (2015) 746-754.

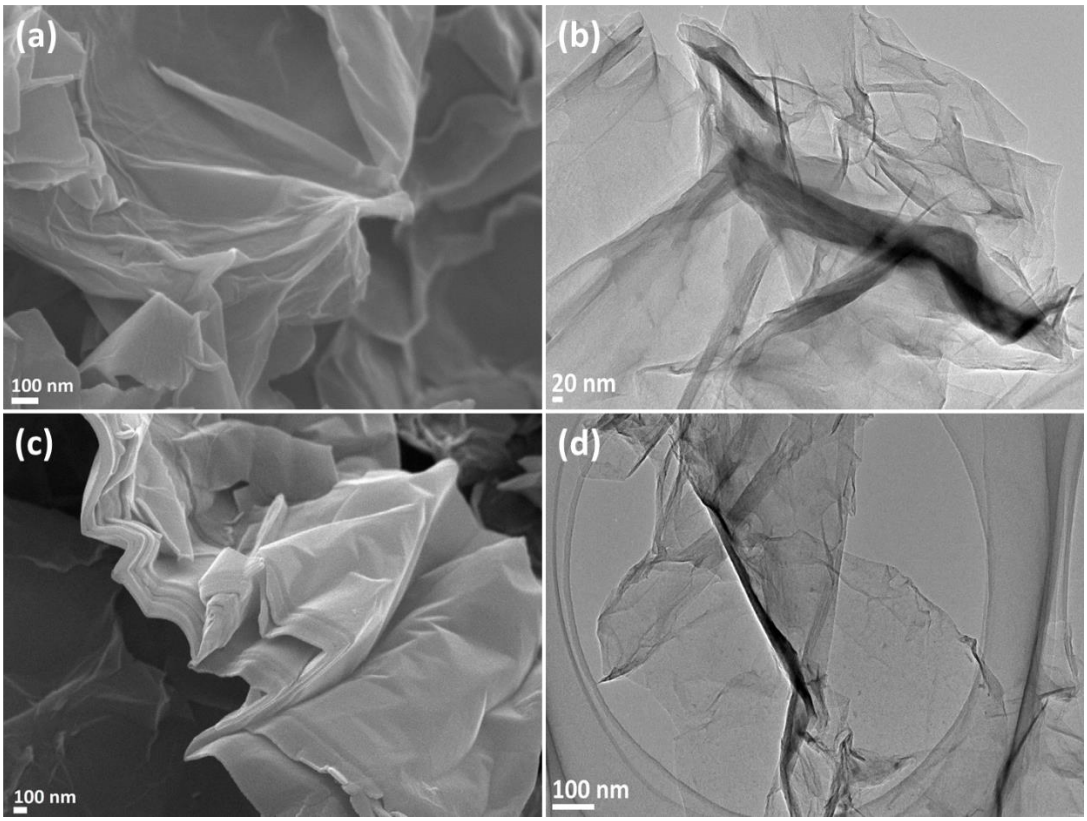

Figure 1 FESEM images (a, c) and TEM images (b, d) of Fe-RGO and Sn-RGO, respectively

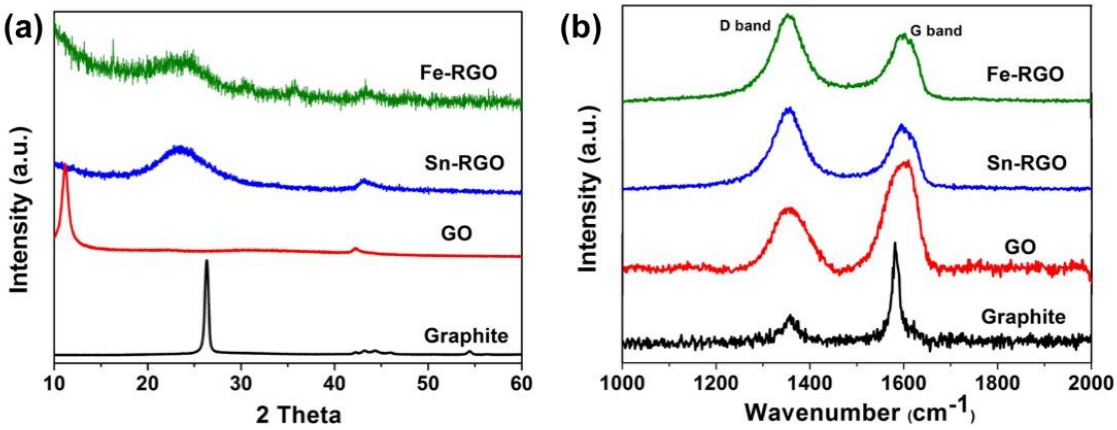

Figure 2 (a) XRD and (b) Raman spectra of graphite, graphene oxide, Sn-RGO and Fe-RGO

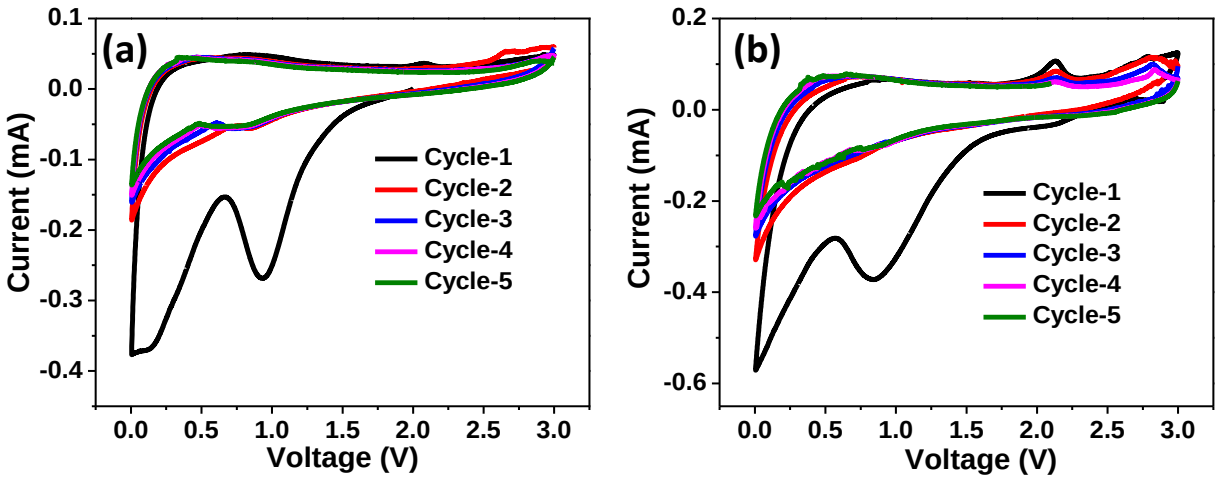

Figure 3 Cyclic voltammograms of (a) Fe-RGO and (b) Sn-RGO

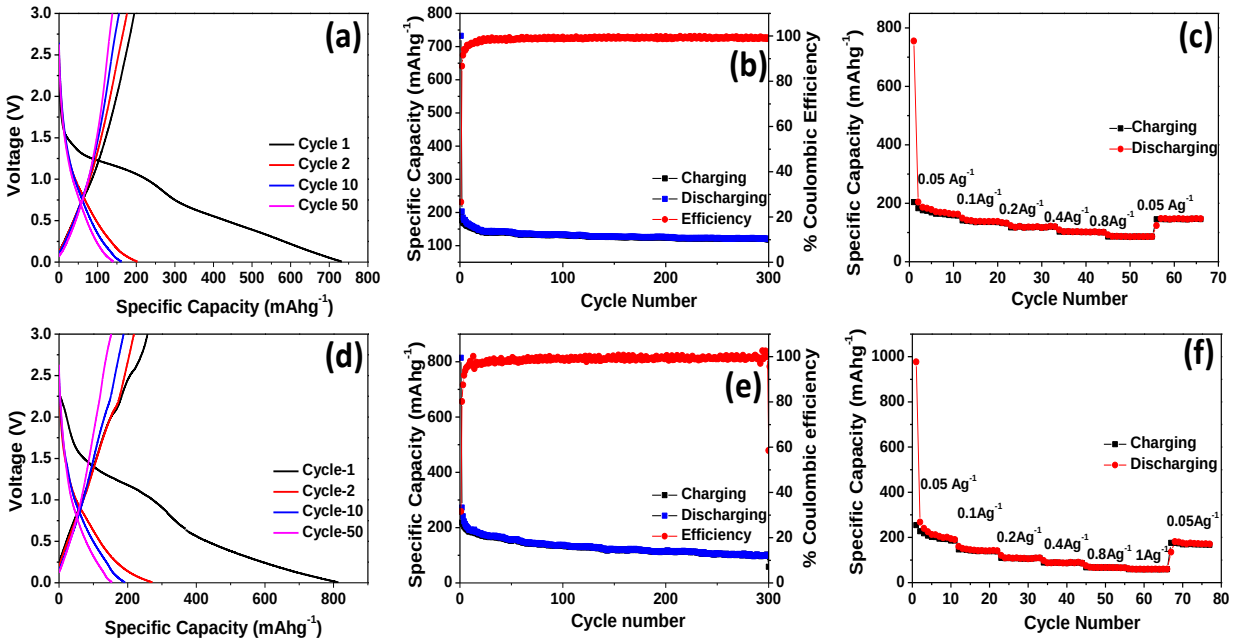

Figure 4. Electrochemical performance of Fe-RGO and Sn-RGO tested against sodium: charge-discharge curves (a, d), cycling stability (b, e), and rate capability (c, f).

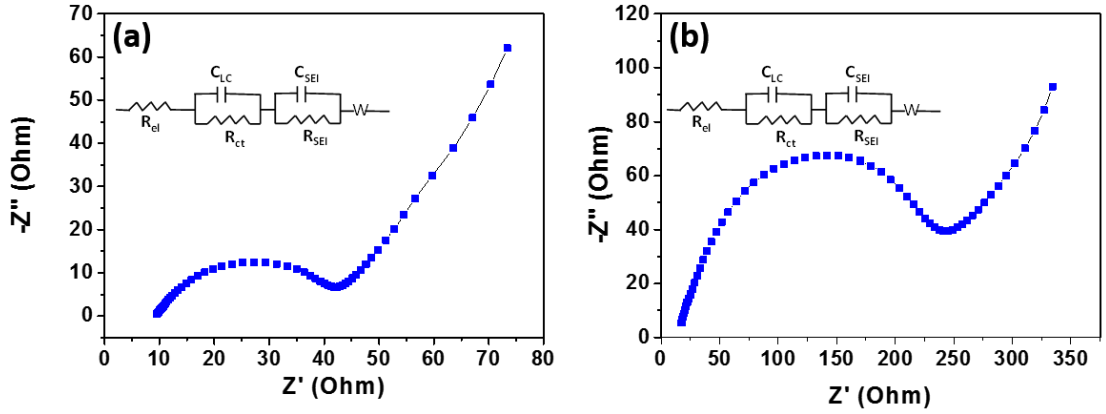

Figure 5 Electrochemical impedance spectroscopy of (a) Fe-RGO and (b) Sn-RGO (Inset: Equivalent circuit)

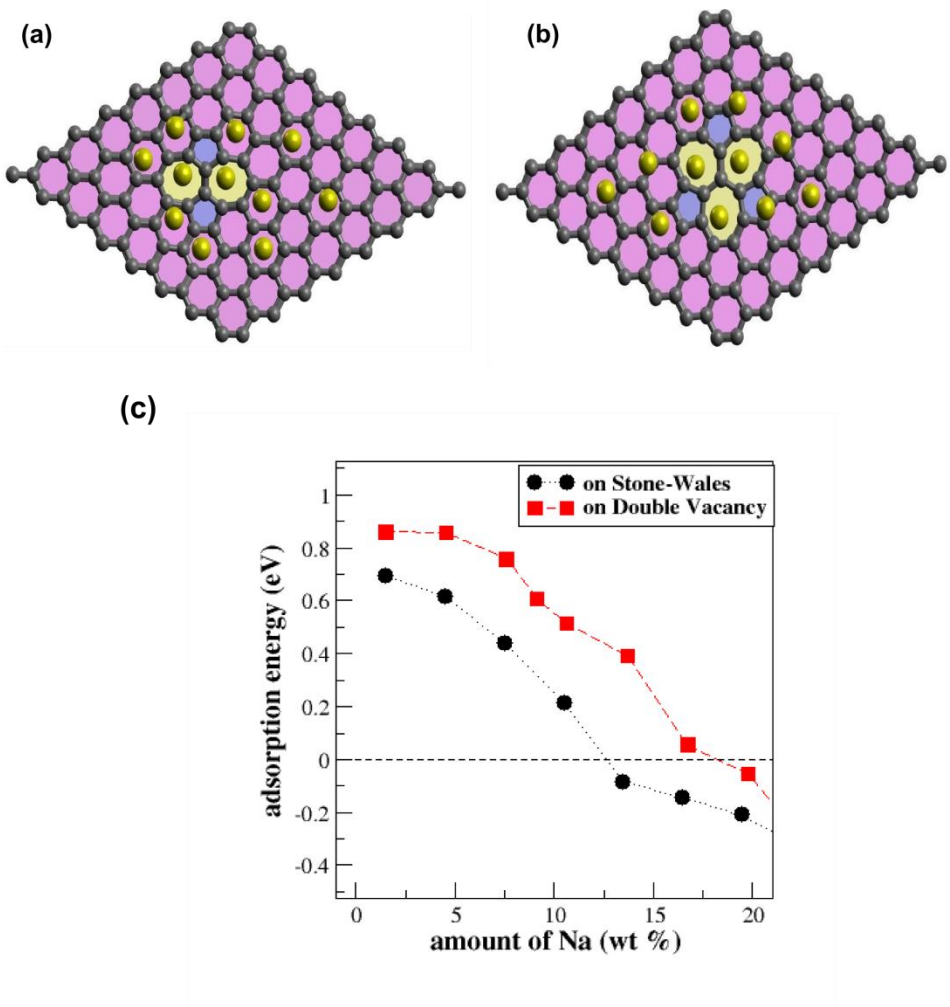

Figure 6 Snapshot depicting adsorbed phase of graphene sheets with one (a) SW (b) DV and Na atoms. Yellow and black spheres represent Na and graphene carbon atoms respectively. Yellow, blue and purple shaded regions represent 8, 5 and 6 membered rings respectively. The average distance between Na atom and the graphene plane is around 2.30 Å. (c) Adsorption energy (calculated from eq. (1)) for different amounts of Na atoms adsorbed on to the graphene sheet with one SW/DV defect.

Table 1. A comparison of the specific discharge capacity of the as prepared RGO anodes with that of previously reported anodes in NIBs.

Material	**Specific Discharge Capacity (mA h g^{-1})**	**Remarks**	**Ref**
Graphene nanosheets	220 at 30 mA g^{-1}	GO prepared by modified Staudenmaier method and reduced at 300 °C in Argon	[17]
Crumpled graphene sheet	183 at 100 mA g^{-1}	Thionyl chloride used as reducing agent followed by heat treatment at 600 °C in Argon	[16]
Reduced graphene oxide	174 at 40 mA g^{-1}	RGOs prepared by heat treatment (450 °C) followed by annealing in N_2 atmosphere at 750 °C	[15]
Expanded graphite	280 at 20 mA g^{-1}	Heat treatment based reduction (600 °C)	[20]
Reduced graphene oxide (free standing paper electrode)	140 at 100 mA g^{-1}	Heat treatment based reduction. (300-900 °C)	[19]
Expanded graphitic material	150 at 37 mA g^{-1}	Heat treatment based reduction (300 °C)	[52]
Reduced graphene oxide	272 at 50 mA g^{-1}	Sn induced GO reduction (RT)	**Present work**
Reduced graphene oxide	202 at 50 mA g^{-1}	Fe induced GO reduction (RT)	**Present work**

[#]RT- Room temperature